J. Fluid Mech. (1998), *vol.* 371, *pp.* 59–79 Printed in the United Kingdom

Motion of inertial spheroidal particles in a shear flow near a solid wall with special application to aerosol transport in microgravity

By EHUD GAVZE[1] AND MICHAEL SHAPIRO[2]†

[1] Israel Institute for Biological Research, PO Box 19, Ness-Ziona 74100, Israel

[2] Laboratory of Transport Processes in Porous Materials, Faculty of Mechanical Engineering, Technion – Israel Institute of Technology, Haifa 32000, Israel

(Received 8 May 1997 and in revised form 26 February 1998)

Trajectories of inertial spheroidal particles moving in a shear flow near a solid wall are calculated numerically from the Stokes flow equations by computing the hydrodynamic forces and torques acting on the particles. Near the wall these interactions cause coupling between the particle's rotational and translational motions. Due to this coupling an inertial spheroid is shown to move along an oscillatory trajectory, while simultaneously drifting towards the wall. This phenomenon occurs in the absence of gravity as a combined effect of three factors: particle non-spherical shape, its inertia and particle–wall hydrodynamic interactions. This drift is absent for inertialess spheroids, and also for inertial spherical particles which move along flow streamlines.

The drift velocity is calculated for various particle aspect ratios γ and relaxation times τ. An approximate solution, valid for small particle inertia is developed, which allows the contribution of various terms to the drift velocity to be elucidated. It was found that the maximum value of the drift velocity prevails for $N(\gamma)\gamma^2\tau s \sim 4$, where s is the shear rate and $N(\gamma)$ is a decreasing function of γ, related to the particle–wall hydrodynamic interactions. In the limiting cases of large and small inertia and also of very long and thin spheroids, the drift vanishes.

Possible applications of the results are discussed in the context of transport of micrometre particles in microgravity conditions. It is shown that the model used is applicable for analysis of the deposition of aerosol particles with sizes above 10 μm inhaled in the human respiratory tract in the absence of gravity.

1. Introduction

The transport of small particles in shear flows is a problem having numerous applications in particle technology and various physiological and biological processes. Most existing treatments pertain to spherical particles, because their geometry allows relatively simple analytical solutions of their equations of motion to be obtained. Non-spherical particles, such as blood cells, asbestos, cotton and wool fibres, clusters and agglomerates are very common in many environmental industrial and physiological processes. The motion of such particles may be fairly complicated, and is characterized by rotation, tumbling, oscillations, drift, etc.

In many situations only the translational transport of non-spherical particles is the objective of the treatment. One way to simplify the calculation of the particle translational trajectory is to replace a non-spherical particle by either of its spherical

† Author to whom correspondence should be addressed.

equivalents, i.e. one of the same volume or drag resistance. It turns out, however, that such modelling of non-spherical particle motion can give results which are wrong in quantitative terms and misleading in physical nature. One such case is the motion of non-spherical particles in shear flows. Particle rotation induced by the shear (Jeffery 1922) may affect significantly its translational motion.

One of the specific subjects which is of interest in many applications is particle transport in rectilinear flows, i.e. in tubes and channels. In the absence of external body forces, or when the flow direction is vertical, it is natural to expect that the suspended particles will move along straight trajectories. Sometimes, however, particles drift across streamlines. The most notable example is the motion of spheroids in vertical uniform flow, where they settle along inclined trajectories due to the gravity force (Happel & Brenner 1983).

Other factors which might be responsible for particle drift in rectilinear flows are particle and fluid inertia and proximity to solid walls. The effect of fluid inertia is responsible for the lateral drift across streamlines of neutrally buoyant spheres in Poiseuille flow (Segré & Silberberg 1962*a*, *b*; Ho & Leal 1974; Schonberg & Hinch 1989) and various non-spherical particles (Karnis, Goldsmith & Mason 1963, 1966). Elliptical cylinders settling in a vertical channel migrate due to the orientational dependence of particle hydrodynamic interactions, induced by fluid inertia (Huang, Feng & Joseph 1994).

Hydrodynamic interactions with solid walls can significantly affect particle motion. A wall retards the rectilinear motion of spheres flowing parallel to its surface. Near the wall non-spherical particles move in a fairly complicated manner even for negligible fluid and particle inertia. In particular, in the absence of body forces inertialess spheroids moving in the shear flow near a solid wall can acquire a non-zero velocity component normal to the wall surface (Gavze & Shapiro 1997). A dramatic effect of particle–wall interactions was demonstrated by Sugihara-Seki (1993). He showed that inertialess elliptical cylinders transported in narrow channels can either tumble or oscillate in their rotational motion, depending on particle/channel aspect ratio. In both cases the particles undergo a considerable side drift towards and from the wall. Similar trajectories were calculated by Yang & Leal (1984) for inertialess slender bodies moving in a shear flow near a fluid–fluid interface.

In the absence of particle and fluid inertia and also body forces, trajectories of spheroidal particles in rectilinear flows near the wall, with all their complexity are, however, periodic. That is, particles on the average move along the channel or tube axis, executing zero net lateral drift. This is no longer true when either particle or fluid inertia is included. Feng & Joseph (1995) showed that fluid unsteady (i.e. associated with the $\partial \boldsymbol{V}/\partial t$ term) and steady inertia ($\boldsymbol{V}\cdot\boldsymbol{\nabla}\boldsymbol{V}$ term) can have accumulating long-time effects on the particle motion. In particular, they showed that the quasi-steady-state tumbling trajectory of inertialess spheroids calculated by Sugihara-Seki is unreachable for comparable inertial particles. Feng & Joseph (1995) also examined the effect of fluid and particle inertia on the rotation of prolate ellipsoids in a simple shear flow far from walls. They found that the particle trajectories differ only slightly from the classical Jeffery orbits of inertialess particles rotating in creeping flow. However, their particles had very small inertia.

It follows thus that the effect of the inertia of non-spherical particle motion cannot be neglected in calculating their trajectories. The motion of such inertial particles near the wall has not been investigated. The objective of this article is to study the effect of inertia on the motion of prolate spheroidal particles in a shear flow near a solid wall in the absence of body forces. Explicitly, we look into the circumstances where the

particle density is much larger than that of the fluid, so that the particle inertia is important and the fluid's inertia is negligible. Physically this situation corresponds to aerosol particles (at normal or reduced air pressure) under microgravity conditions. There is a continuing interest in the investigation of aerosol process in microgravity because of the many fundamental physical phenomena, environmental and physiological processes and potential industrial applications related to aerosol processing (Holländer 1993, 1996; Oostra *et al.* 1995, 1996).

We first address the problem of the particle motion far from the wall. The particle centre of mass remains always at the same distance from the wall, but the rotational motion strongly depends upon the particle inertia. Analysis of this motion helps to understand the particle motion in the vicinity of the wall, which is the main goal of this paper. Comparable inertialess particles in similar circumstances tumble along oscillatory trajectories while periodically approaching and departing from the wall surface. In such a motion even slight particle inertia can cause particle drift across the streamlines. We show that for prolate spheroids such a drift does indeed occur in the direction towards the wall which ultimately leads to their deposition on the wall surface.

2. Model

Consider a simple shear flow $U = sz$, characterized by shear rate s, of a fluid with viscosity μ in the plane semi-infinite region $z > 0$, over a flat wall $z = 0$ (see figure 1). Let a prolate spheroidal particle with semi-axes $a < c$ and uniformly distributed mass m be immersed in this flow. We assume that diffusion, gravity and other external forces are absent. The flow velocity field and trajectories of a spheroid are described by the following equations:

$$\rho(\partial \boldsymbol{V}/\partial t + \boldsymbol{V}\cdot\boldsymbol{\nabla}\boldsymbol{V}) = -\boldsymbol{\nabla}p + \mu\nabla^2\boldsymbol{V}, \tag{1a}$$

$$\boldsymbol{\nabla}\cdot\boldsymbol{V} = 0, \tag{1b}$$

$$m\mathrm{d}\boldsymbol{v}/\mathrm{d}t = \boldsymbol{F}, \tag{2}$$

$$\boldsymbol{I}\mathrm{d}\boldsymbol{\omega}/\mathrm{d}t - \boldsymbol{I}\boldsymbol{\omega}\times\boldsymbol{\omega} = \boldsymbol{L}, \tag{3}$$

$$\boldsymbol{V} = \boldsymbol{0} \quad \text{at} \quad z = 0, \tag{4a}$$

$$\boldsymbol{V} = \boldsymbol{i}_x sz, \quad |\boldsymbol{r}| \to \infty, \tag{4b}$$

$$\boldsymbol{V} = \boldsymbol{v} + \boldsymbol{\omega}\times\boldsymbol{r} \quad \text{on the particle surface}, \tag{4c}$$

where $\boldsymbol{r}$ is the position vector in the particle-fixed coordinate frame, $\boldsymbol{V}$ and p are the fluid velocity and pressure, respectively, ρ and μ are the fluid mass density and dynamic viscosity, $\boldsymbol{v} = (u, w)$ and $\boldsymbol{\omega}$ are the translational velocity of its centre and its rotational velocity respectively, $\boldsymbol{I}$ is its inertia tensor, and $\boldsymbol{F}$, $\boldsymbol{L}$ are the hydrodynamic force and torque experienced by the spheroid in the fluid. These interactions are expressible via the hydrodynamic stresses prevailing on the particle surface.

We assume that the particle is sufficiently small so that the characteristic Reynolds number $Re = sc^2/\nu \quad 1$, where $\nu = \mu/\rho$ is the fluid kinematic viscosity. That is, the perturbation of the flow field induced by the particle motion is described by the quasi-steady creeping flow Stokes equations. These are obtained by dropping the inertia terms $\partial \boldsymbol{V}/\partial t$ and $\boldsymbol{V}\cdot\boldsymbol{\nabla}\boldsymbol{V}$ in (1*a*):

$$\mu\nabla^2\boldsymbol{V} = \boldsymbol{\nabla}p, \quad \boldsymbol{\nabla}\cdot\boldsymbol{V} = 0. \tag{5a,b}$$

For simplicity we assume that the particle moves in the plane $y = \text{const.}$, so that at any time its position can be described by the Cartesian coordinates (x, z) and the angular

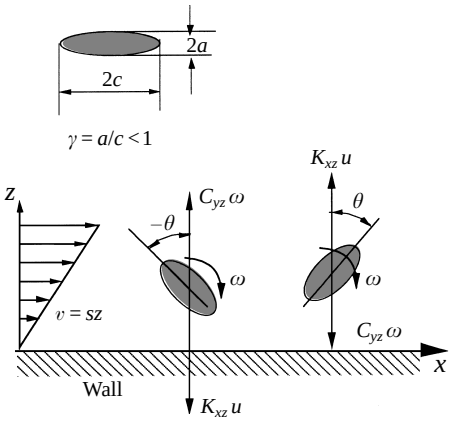

FIGURE 1. A spheroidal particle moving in a simple shear flow near a wall. Schematic of the flow arrangement.

coordinate θ. In these circumstances, the particle motion in the inertial coordinate system can be described by the following system of equations (Gavze & Shapiro 1997):

$$\frac{\mathrm{d}}{\mathrm{d}t}\begin{bmatrix} mu \\ mw \\ I_{yy}\omega \end{bmatrix} = \begin{bmatrix} F_x \\ F_z \\ L_y \end{bmatrix} - \boldsymbol{R}\begin{bmatrix} u \\ w \\ \omega \end{bmatrix}, \quad \begin{bmatrix} u \\ w \\ \omega \end{bmatrix} = \frac{\mathrm{d}}{\mathrm{d}t}\begin{bmatrix} x \\ z \\ \theta \end{bmatrix}; \tag{6a,b}$$

In the above I_{yy} is the yy-component of the particle inertia tensor, $\boldsymbol{R} = \boldsymbol{R}(x, z, \theta)$ is the position- and orientation-specific resistance matrix of a spheroid moving in a quiescent fluid near a wall, and F_x, F_z, L_y, are the corresponding components of the hydrodynamic viscous drag force and torque, experienced by a spheroid fixed in a shear flow near a wall. The resistance matrix is calculated from the hydrodynamic stresses. These are obtained from the solutions of the creeping flow equations (5a, b), when the particle moves with unit velocities in the respective directions x, z, θ, in an otherwise quiescent fluid subject to the condition of vanishing velocity at infinity. The particle resistance matrix in the present case has the following form (Gavze & Shapiro 1997):

$$\boldsymbol{R} = \mu\begin{bmatrix} K_{xx} & K_{xz} & C_{yx} \\ K_{xz} & K_{zz} & C_{yz} \\ C_{yx} & C_{yz} & \Omega_{yy} \end{bmatrix} \tag{7}$$

where $K_{\alpha\beta}(\alpha, \beta = x, z)$ are elements corresponding to the translational motion, Ω_{yy} pertains to the particle rotational motion, and, finally C_{yx}, C_{yz}, are elements (of the coupling tensor $\boldsymbol{C}$) describing coupling between the particle translation and rotation.

The hydrodynamic interactions F_x, F_z, L_y are calculated by application of the reciprocal theorem (Happel & Brenner 1983) to the hydrodynamic stresses acting on the particle in a quiescent fluid and to the flow in which it is immersed, i.e. the simple shear flow. Calculation of the above stresses, which is the most time-consuming task, is done once for all subsequent calculations on a discrete grid in z, θ space by the boundary element method (Gavze & Shapiro 1997). The values of the elements of the resistance matrix, as well as the hydrodynamic interactions at intermediate points, needed for the integration of equation of motions, are interpolated from the grid points. Integration of the equations of particle motion by this method is extremely efficient and requires a negligible computation time compared to other methods in which the Navier–Stokes equations are subsequently solved, following the particle motion.

For axisymmetrical particles considered here, confined to the plane $y = \text{const.}$, the only relevant component of the inertia tensor is $I_{yy} = m(a^2+c^2)/5$. The set of rotational equations reduces to a single equation of rotation with respect to the y-axis, coupled with the equations of the translational motion.

Define the following dimensionless quantities, designated below by primes:

$$\left.\begin{array}{l} x' = x/c, \quad z' = z/c, \quad t' = ts, \quad \theta' = \theta, \\ K'_{\alpha\beta} = K_{\alpha\beta}/c, \quad C'_{\alpha\beta} = C_{\alpha\beta}/c^2, \quad \Omega'_{\alpha\beta} = \Omega_{\alpha\beta}/c^3, \\ u' = u/cs, \quad w' = w/cs, \quad \omega' = \omega/s, \\ F'_\alpha = F_\alpha/\mu sc^2, \quad L'_\alpha = L_\alpha/\mu sc^3. \end{array}\right\} \tag{8}$$

Using the above one can rewrite (6a) in the dimensionless form

$$\gamma^2\tau s\frac{\mathrm{d}}{\mathrm{d}t'}\begin{pmatrix} u' \\ w' \\ (1+\gamma^2)\,\omega'/5 \end{pmatrix} = \begin{pmatrix} F'_x \\ F'_z \\ L'_y \end{pmatrix} - \boldsymbol{R}'\begin{pmatrix} u' \\ w' \\ \omega' \end{pmatrix}, \quad \begin{bmatrix} u' \\ w' \\ \omega' \end{bmatrix} = \frac{\mathrm{d}}{\mathrm{d}t'}\begin{bmatrix} x' \\ z' \\ \theta' \end{bmatrix}. \tag{9}$$

In the above τ is the particle characteristic relaxation time:

$$\tau = \tfrac{4}{3}\pi\frac{\rho_p\, c^2}{\mu}, \tag{10}$$

where ρ_p is the particle mass density. The product τs characterizes the particle inertial properties, similarly to the Stokes number, used when a characteristic value of flow or particle velocity is prescribed. The complex τs and the particle aspect ratio $\gamma = a/c$ are the dimensionless quantities governing its rotational and translational motions via the basic set of equations (9); γ is implicitly included in these equations also via the elements of the matrix $\boldsymbol{R}'$ and the forces F'_x, F'_z and L'_y. Note that $\tau s = (4\pi/3)Re\rho_p/\rho$, which means that for the small Re considered here, large τs values are obtained when the density ratio ρ_p/ρ greatly exceeds unity. This condition implies that the body forces are normally important in the analysis of the particle motion (see Broday *et al.* 1998; Gavze & Shapiro 1996). Nevertheless, in the present work the body forces are omitted, so we concentrate on the role of particle inertia, its non-spherical shape and particle–wall hydrodynamic interactions (see §7 for a discussion on this matter).

In the following we omit the primes for the sake of convenience. It follows from (9) that each of the functions x, z, θ governing particle trajectories may be represented in the following dimensionless form: $f(t, z_0, x_0, \theta_0, \gamma, \tau_s)$, where the set $(x_0 = 0, z_0, \theta_0)$ characterizes particle initial location and orientation.

With quantities F_x, F_z, L_y determined from the solutions of the pertinent creeping flow problems, (9) are numerically integrated by the Runge–Kutta method for various initial distances z_0, orientation angles θ_0, aspect ratios and inertia parameters. The ultimate goal of the calculations is the determination of the trajectories traced by the spheroids' centres of mass. The orientations are explicitly calculated at each integration step in order to determine the (θ-dependent) corresponding forces and torque, as well as the velocity components. Moreover, in cases where the particle ultimately touches the wall, its orientation is necessary for calculating the terminal configuration (stopping distance). The calculations terminate when the distance between the particle surface and the wall is less than $0.01c$.

3. Results

Figure 2(a, b) presents trajectories of the particles' centres of mass vs. dimensionless time t. In creeping flow spherical particles flowing near the wall move along the flow

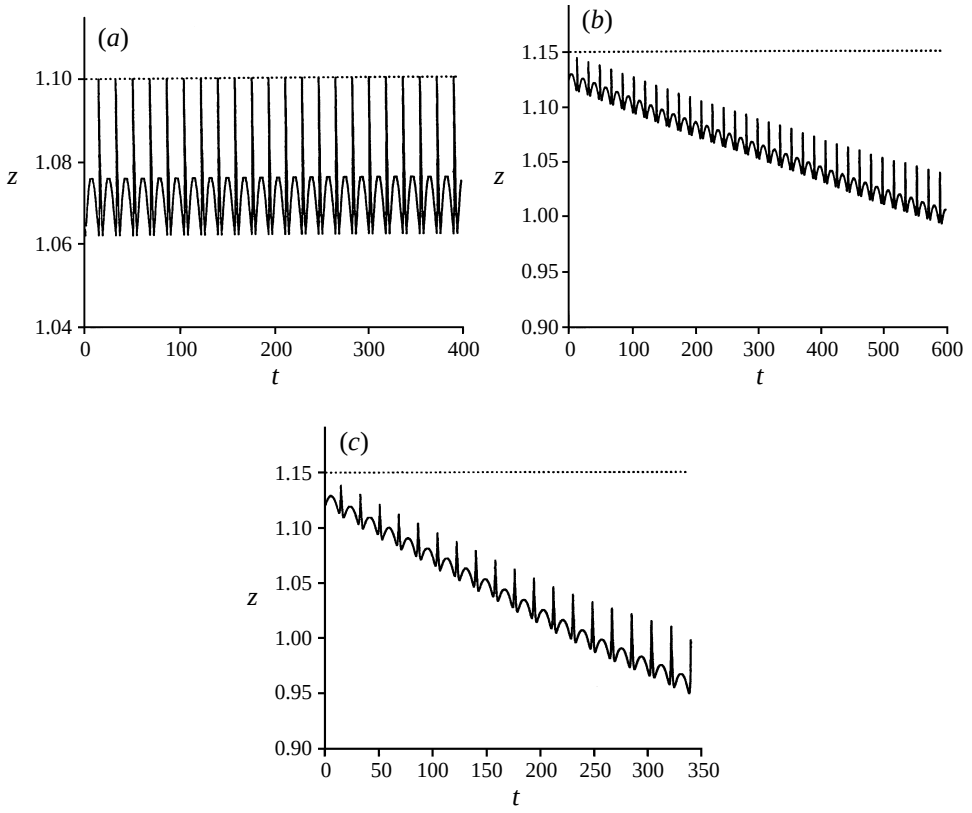

FIGURE 2(*a–c*). For caption see facing page.

streamlines. So do inertialess ($\tau s = 0$) spheroidal particles far from the wall (see figure 2*a*, dotted line). In the vicinity of the wall these particles execute oscillatory translational–rotational motion, namely, beginning from any initial location and orientation, their centres move periodically, with their average distance from the wall being constant (see figure 2*a*).

Inertial spheroidal particles in the wall vicinity move in a different manner. They rotate and move along oscillatory trajectories, while gradually drifting towards the wall. This pattern is found to be independent of the initial orientation and distance z_0 from the wall. The rate of particle drift towards the wall depends on the parameters γ and τs, as well as on the local distance z.

The role of the particle inertia may be observed by comparing figures 2(*b*) and 2(*c*) both showing the trajectories of particles of the same aspect ratio, which begin their motion from the same location. One can see in figure 2(*c*), that the particle with larger inertia ($\tau s = 100$) hits the wall at about $t = 350$, whereas the less inertial particle (with $\tau s = 50$) has not reached the wall even at $t = 600$.

The role of the particle aspect ratio may be elucidated by observing figures 2(*c*) and 2(*d*). The particle with $\gamma = 0.5$ (see figure 2*d*), drifts much faster than does the more elongated particle of the same inertia (see figure 2*c*). Therefore the rate of drift decreases with decreasing γ. This accords with the results of the analyses of the particle–wall interactions (Gavze & Shapiro 1997), namely, with decreasing particle aspect ratio the wall effect diminishes. Moreover, the rotational period of the more elongated particle is much longer and the amplitude of its vertical oscillations is smaller

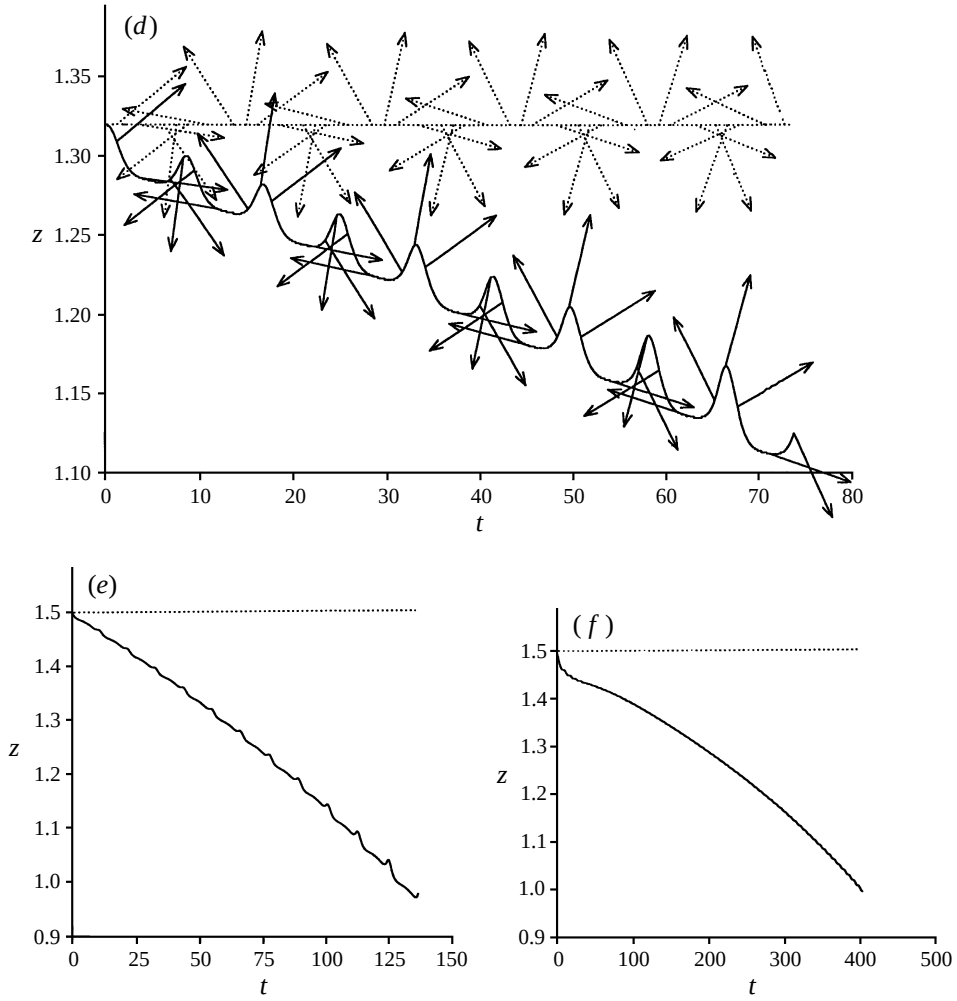

FIGURE 2. Trajectories of centres of spheroidal particles in a shear flow near a wall. Dotted line is the solution far from the wall. Solid line is the solution near the wall. (*a*) $\gamma = 0.2$, $\tau s = 0$; (*b*) $\gamma = 0.2$, $\tau s = 50$; (*c*) $\gamma = 0.2$, $\tau s = 100$; (*d*) $\gamma = 0.5$, $\tau s = 100$; (*e*) $\gamma = 0.2$, $\tau s = 500$; (*f*) $\gamma = 0.2$, $\tau s = 5000$. Arrows in (*d*) show orientations of the particle longer axis at the time moments corresponding to their rear edges.

than the comparable quantities of its less elongated counterpart. Increasing particle aspect ratio beyond 0.5 ultimately results in a slower particle drift, since the particle shape approaches spherical in which case the drift vanishes. With γ fixed, increasing inertia parameter τs leads to an increase of the drift rate (see figure 2*c*, *e*). However, beyond a certain critical value of τs of about 500 the drift rate decreases (see figure 2*e*, *f*).

Figure 2 (*d*) shows the evolution of the spheroid's orientation during its approach to the wall. The spikes in the z-coordinate correspond to an almost vertical orientation, where θ is about 15°. The period of rotation near the wall is larger than far from the wall.

The above results are summarized in figures 3 and 4, showing the non-dimensional drift velocity w_d. In the vicinity of the wall this quantity is a weak function of the distance z (see figure 3). The drift increases as the particle approaches the wall. In the range $\tau s < 80$, w_d as a function of γ has a maximum at $\gamma \sim 0.5$–0.6 (see figure 4). That

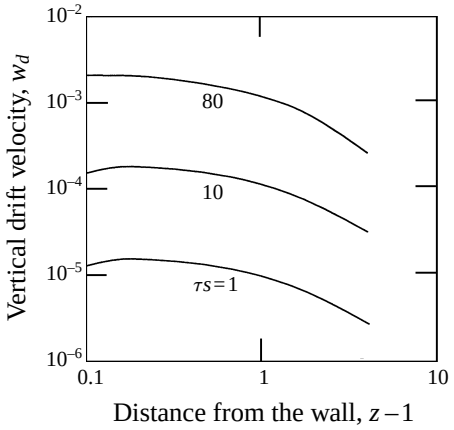

FIGURE 3. Vertical drift velocity vs. particle distance from the wall, $a/c = 0.5$.

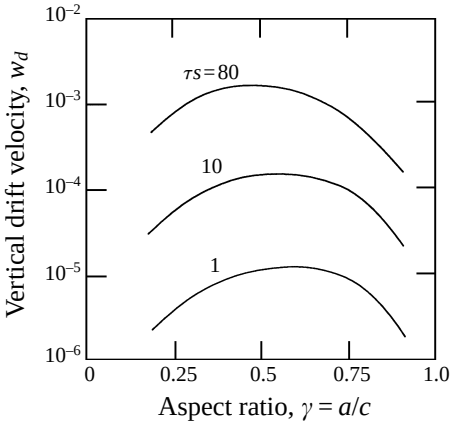

FIGURE 4. Vertical drift velocity vs. particle aspect ratio, $z = 1.5$.

is, the drift velocity decreases with particle geometry approaching spherical. It also decreases with decreasing γ in the limit of oblong particles in accordance with force analyses of Gavze & Shapiro (1997). Also, w_d in this range of inertia parameter exhibits a linear dependence on τs (see a discussion on this matter below).

Figure 5 presents w_d as a function of $\gamma^2\tau s$. This parameter appears in (11) of §4 as a dimensionless coefficient multiplying the acceleration term. In this plot w_d has maxima for all γ at about $\gamma^2\tau s \sim 40$–50, with the absolute maximum value prevailing at about $\gamma \sim 0.2$–0.3. Several calculated values of the drift velocity are presented in table 1.

The set of curves plotted in figure 5 shows that in the two extremes (i) $\gamma^2\tau s \gg 1$ and (ii) $\gamma^2\tau s \ll 1$ the effect of inertia and shape on w_d are lumped within a sole parameter $\gamma^2\tau s$. This may be rationalized in the following way. The first limit (i) may be rewritten in the form $\tau s \gg 1$, γ-fixed. In this case of very large inertia, the particle dynamics is entirely determined by its rotational inertia. Below we show (see the Appendix) that this is measured by $\gamma^2\tau s$, which may be interpreted as the dimensional relaxation time of the particle rotational motion. We also show that in this extreme the particle rotates with a constant rotational velocity which differs very little from its value $s/2$ prevailing far from the wall. The effect of the wall on such rotational motion is relatively weak, which results in a slow velocity drift.

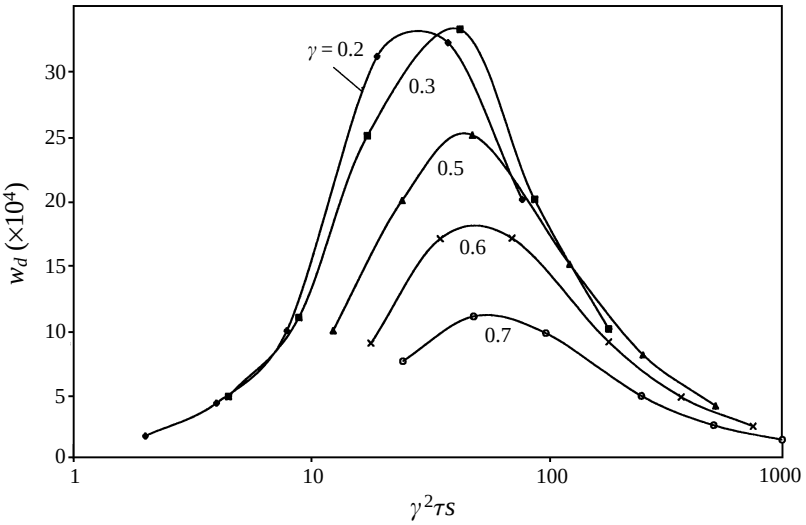

FIGURE 5. Vertical drift velocity vs. inertia parameter, $z = 1.5$.

γ	$\tau s = 50$	$\tau s = 100$	$\tau s = 200$	$\tau s = 500$	$\tau s = 1000$	$\tau s = 2000$
0.2	1.9	4.4	10	31	32*	20
0.3	4.9	11	25	33*	20	10
0.5	10	20	25*	15	8.0	4.0
0.6	9.0	17*	17	9.0	4.7	2.4
0.7	7.6	11*	9.7	4.8	2.5	1.3
0.9	1.2	1.5	1.1	0.5		

TABLE 1. Dimensionless drift velocity $10^4 w_d$ at $z = 1.5$. Starred values corresponds to $\gamma^2 \tau s \sim 40$–50.

The opposite limit (ii) can be realized by the two situations: $\gamma \gg 1$, τs-fixed, and $\tau s \gg 1$, γ-fixed. In the first of these cases the particle is very long/thin, in which circumstances the wall effect is weak (Gavze & Shapiro 1997) and the effect of the shape parameter is lumped within a parameter proportional to $\gamma^2 \tau s$ (see the Appendix). The other situation, namely $\tau s \gg 1$, γ-fixed, describes very light (almost inertialess) particles, characterized by small drift velocities, the rotational motion of which is affected by a single relaxation parameter $\gamma^2 \tau s$ (see the Appendix).

We thus conclude that the largest drift velocities prevail for the intermediate values of $\gamma^2 \tau s$, where in addition to this parameter, w_d is also affected by the aspect ratio γ via the hydrodynamic viscous interactions. The limiting cases of large and small inertia and also of very long spheroids described above pertain to situations where the drift is relatively slow.

Note that the approach of a spherical particle towards the plane wall is accompanied by the so-called lubrication effect, which is an indefinite increase of the resistance force F_z, caused by squeezing the viscous liquid out of the particle–wall gap. In contrast to the sphere, the approach to the wall of a rotating spheroid is governed by four forces F_z, $K_{xz} u$, $C_{yz} \omega$ and $K_{zz} w$. In our earlier paper (Gavze & Shapiro 1997) we showed that F_z, K_{xz}, C_{yz} and K_{xz} all increase as the particle approaches the wall like $1/z$. Some of these terms act in the wall direction and some in the opposite direction. The drift w_d arises from the fact that the above forces are not balanced on the average. Alternative interpretations and analyses of this phenomenon are given in the following sections.

We also calculated other parameters of the particle trajectory, namely the oscillation period and the amplitude. In particular, the dimensionless period is found to be a weak function of the inertia parameter τs and the distance z. The oscillation amplitude was found to increase with the particle approaching the wall. Further discussion of the effects of these parameters is given in §4.

4. Discussion of the results

The drift of spheroidal particles described in the previous section is a phenomenon arising from three basic factors: (i) the particle's non-spherical form, (ii) its inertia and (iii) coupled hydrodynamic interactions with the wall. All particles immersed in a shear flow rotate. However, a spheroidal particle moving in the vicinity of a solid wall acquires a velocity component perpendicular to its surface (Gavze & Shapiro 1997).

In the following we concentrate on the effect of inertia on particle rotational motion, which provides a clue towards understanding of the drift phenomenon. Consider, first the particle motion far from the wall, where the components C_{yx}, C_{yz} of the coupling tensor $\boldsymbol{C}$ vanish, and translational and rotational motions are uncoupled. The expressions for the non-vanishing terms of the tensor $\boldsymbol{K}$, as well as for the force and torque, may be found in Gavze & Shapiro (1997). Far from the wall the solution $u = z, w = 0$, valid for inertialess particles, also satisfies the translational equations of system ((11) below), written for inertial spheroids, but only for a sufficiently long time $t \quad \tau s$. The rotational equation far from the wall has the form (see the Appendix)

$$\tau s A(\gamma)\frac{\mathrm{d}^2\theta}{\mathrm{d}t^2}+\frac{\mathrm{d}\theta}{\mathrm{d}t}=\frac{1}{2}\left(\frac{1-\gamma^2}{1+\gamma^2}\cos 2\theta+1\right), \tag{11}$$

where $A(\gamma)$ is a non-dimensional constant. In the inertialess case $\tau s = 0$ and the solution of (11) is (Jeffery 1922)

$$\omega=\frac{1}{2}\left(1+\frac{1-\gamma^2}{1+\gamma^2}\cos 2\theta\right), \quad \theta(t)=\arctan\left[\frac{1}{\gamma}\tan\left(\frac{\gamma t}{1+\gamma^2}\right)\right]. \tag{12}$$

Unlike the comparable solution for the translation motion, this one does not constitute a limit cycle of (11). The solution of (11) with inertia included is of particular importance, for it does not differ much from the solution of the angular equation of system (9), in the region close to the wall. Asgharian & Anjilvel (1995) solved the equations of particle rotation analogous to (11) in the absence of the wall. Here we, in addition, present the solution of the full set of equations (9) near the wall for various values of $z, \tau s$ and γ.

Figure 6 presents the limit cycle of ω vs. θ calculated for $\gamma = 0.5$ from (11) (figure 6*a*, *b*), as well as from the solution of the full system (9) near the wall at $z = 1.15$ (figure 6*c*, *d*). One can observe a minor difference between the corresponding solutions far from and near the wall, although this difference evolves as the particle drifts towards the wall.

For each value of $\cos(2\theta)$ there exist two values of ω in figure 6. The upper branches correspond to positive θ and the lower branches to negative θ. For $\tau s \sim 10$ the asymmetry of the w, θ curve, as measured by the difference $\Delta\omega = \omega(\theta)-\omega(-\theta)$ between the corresponding values of ω belonging to these two branches is negligible. In this case the slopes of both branches are close to the value $0.5(1-\gamma^2)/(1+\gamma^2)$ prevailing for inertialess particles (see (12)). As τs increases, so do the asymmetry and $\Delta\omega$, until the latter reaches its maximum at about $\tau s = 100$–200 for $\gamma = 0.5$ and $\tau s = 500$–1000 for

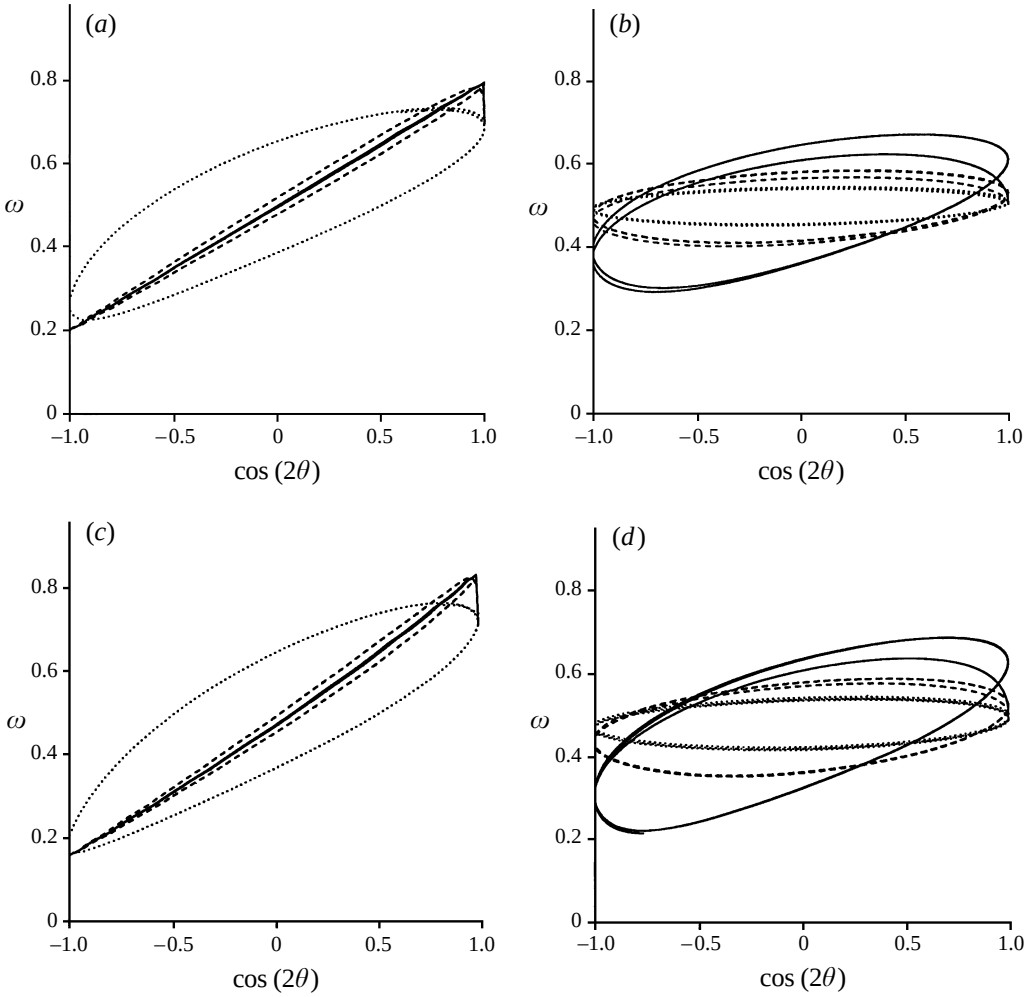

FIGURE 6. Particle rotational velocity far from the wall (a, b), and near the wall, $z = 1.15$ (c, d), vs. orientation angle. $\gamma = 0.5$. (a, c) Solid line, $\tau s = 1$; broken line, $\tau s = 10$; dotted line, $\tau s = 100$. (b, d) Solid line, $\tau s = 200$; broken line, $\tau s = 500$; dotted line $\tau s = 1000$.

$\gamma = 0.2$, both corresponding to $\gamma^2 \tau s \sim 20$–50. Beyond this value of $\gamma^2 \tau s$, $\Delta\omega$ decreases again, together with the inclination slope of both branches. Physically this means that an inertial rotating particle after passing the perpendicular (with respect to the wall), or 'upright', orientation $\theta = 0$ will not regain its angular velocity, which prevailed for $\theta < 0$. This is in contrast with the behaviour of inertialess spheroids, which always remain in equilibrium with the fluid. It thus follows that the inclination asymmetry of ω is maximal at $\gamma^2 \tau s \sim 20$–50. In addition, as the inertia parameter increases beyond this value, ω gradually becomes independent of θ (see figure 6*b*) and approaches 0.5 for all γ. It turns out that the asymmetry of ω, θ curve is related to the rate of particle drift towards the wall (see §5).

For inertialess particles near a wall $\Delta\omega = 0$, and no drift occurs. As long as the inertia is in the range $\gamma^2 \tau s \approx 20$–$50$ the asymmetry of the curve $\omega - \cos 2\theta$ combined with the asymmetry of w, stemming from the effect of the wall, yields the drift. With increasing inertia parameter, ω becomes weakly dependent on θ, $\Delta\omega$ diminishes, the drift slows down and the amplitude of the z-oscillations decreases (see figure 2*f*). The

diminution of $\Delta\omega$ can be explained by noting that a heavy particle cannot significantly change its angular velocity and its rotational pattern approaches a steady rotation (with $\omega = s/2$ far from the wall). As such, indefinite increase of τs will not cause any further change of ω. This leads to the diminution of the asymmetry of the $\omega - \cos 2\theta$ curve and to a decrease of the drift velocity w_d (see figure 5).

Far from the wall and in the limit of small γ the effect of particle shape is lumped within the parameter $\tau s A(\gamma)$ (see Appendix A). The same is true in the limit of large τs with $\gamma = \text{const.}$, since the rotational velocity approaches a constant value, which is independent of γ. In the limit of small γ, $A(\gamma)$ is proportional to γ^2 (see the Appendix). The rotation of spheroids near the wall (and also their drift velocity w_d) is governed by a similar parameter, namely $\gamma^2 \tau s N(\gamma)$, where the function $N(\gamma)$ includes the effect of particle–wall interactions (see (14)–(16) below).

5. Approximate solution for small inertia

To get deeper insight into the mechanism responsible for the particle drift, we investigate the solution of system (9) for small inertia. Towards this goal we construct a solution in the form of an expansion in a power series of a small parameter ε, proportion to $\gamma^2 \tau s$, to be explicitly found below. Define the following vectors:

$$\boldsymbol{F} = \begin{pmatrix} F_x \\ F_z \\ L_y \end{pmatrix}, \quad \boldsymbol{V} = \begin{pmatrix} u \\ w \\ \omega \end{pmatrix}, \quad \boldsymbol{X} = \begin{pmatrix} x \\ z \\ \theta \end{pmatrix},$$

respectively representing particle generalized forces, velocities and location, and a square matrix $\boldsymbol{G}$

$$\boldsymbol{G} = \begin{pmatrix} 1 & 0 & 0 \\ 0 & 1 & 0 \\ 0 & 0 & (1+\gamma^2)/5 \end{pmatrix}.$$

In terms of these quantities, the system (9) may be rewritten in the form

$$\gamma^2 \tau s \boldsymbol{R}^{-1} \boldsymbol{G} \frac{\mathrm{d}\boldsymbol{V}}{\mathrm{d}t} = \boldsymbol{R}^{-1} \boldsymbol{F} - \boldsymbol{V}, \quad \mathrm{d}\boldsymbol{X}/\mathrm{d}t = \boldsymbol{V}. \tag{13a,b}$$

The smallness of the particle inertia should be described both in terms of the parameter $\gamma^2 \tau s$ and the matrix $\boldsymbol{R}^{-1}\boldsymbol{G}$. The value of the latter is characterized by its scalar norm. For this purpose we further use the maximum norm, generically defined for any square matrix $\boldsymbol{A}$:

$$\|\boldsymbol{A}\| = \max_{i=1,2,3} \sum_{j=1}^{3} |A_{i,j}|,$$

where i,j are the indices of the rows and the columns of $\boldsymbol{A}$, respectively.

Let $N(\gamma)$ be the upper bound of the norm of the matrix $\boldsymbol{R}^{-1}\boldsymbol{G}$ in the domain of variation of z, θ, namely $0 < z < \infty$, $-\pi/2 < \theta < \pi/2$. Using the above we now define a normalized resistance matrix

$$\boldsymbol{R}_N = N(\gamma)\boldsymbol{R}, \tag{14}$$

which satisfies the inequality $\|\boldsymbol{R}_N^{-1}\boldsymbol{G}\| \leqslant 1$, and allows (13$a$) to be rewritten in the form

$$\varepsilon \boldsymbol{R}_N^{-1} \boldsymbol{G} \frac{\mathrm{d}\boldsymbol{V}}{\mathrm{d}t} = \boldsymbol{R}^{-1} \boldsymbol{F} - \boldsymbol{V}, \tag{15}$$

γ	$N(\gamma)$	$\gamma^2 N(\gamma)$	$\tau s\|_{\varepsilon=1} = \gamma^{-2}N^{-1}(\gamma)$
0.2	0.154	0.00615	163
0.3	0.123	0.011	90
0.5	0.088	0.022	45
0.6	0.0769	0.0277	36
0.7	0.0681	0.0334	30

TABLE 2. Values of $N(\gamma)$, and $\gamma^2 N(\gamma)$.

with the non-dimensional parameter ε identified as

$$\varepsilon = \gamma^2 N(\gamma)\,\tau s. \tag{16}$$

Table 2 presents several values of $N(\gamma)$, and $\gamma^2 N(\gamma)$.

The right-hand column in table 2 shows the value of τs for which the parameter ε equals unity. Taking unity as an estimate of the radius of convergence of the small-ε expansion solution, to be developed below, one can see that this solution is valid for cases where τs may not be small.

The introduction of the function $N(\gamma)$ and the above definition of ε clarify the effect of the particle shape on its dynamics. This effect cannot be described only in terms of the dimensionless parameter $\gamma^2\tau s$, since γ is also implicitly embodied within the matrix $\boldsymbol{R}$. Indeed, the same value of $\gamma^2\tau s$ may correspond in one case to a spherical particle ($\gamma = 1$, no drift), and also to a spheroid, in which case $w_d \neq 0$. A physically meaningful dimensionless form of the equation of motion is (15), rather than the first of (9) wherein the effect of inertia is represented by the parameter $\varepsilon = N(\gamma)\,\gamma^2\tau s$. To support this conjecture we considered the data shown in figure 5 in the form w_d versus ε. As a result, we found that the maximum drift velocity prevails at about $\varepsilon = N(\gamma)\,\gamma^2\tau s \approx 4$. For all γ checked, the maximum value of w_d diminishes with increasing γ and eventually vanishes at $\gamma = 1$.

Assume now that $\boldsymbol{V}$ may be expanded in the power series of ε:

$$\boldsymbol{V}(t, \boldsymbol{X}, \varepsilon) = \sum_{i=0}^{\infty} \varepsilon^i \boldsymbol{V}^{(i)}(t, \boldsymbol{X}), \tag{17}$$

where $\boldsymbol{V}^{(i)}$ ($i = 0, 1, 2 \ldots$) are functions to be determined. Substitution of (17) into (15) yields the following equation for the zero-order solution $\boldsymbol{V}^{(0)}$:

$$\boldsymbol{R}\boldsymbol{V}^{(0)} = \boldsymbol{F},$$

which implies that $\boldsymbol{V}^{(0)}$ is the velocity of inertialess particles.

The higher-order members of (17) satisfy the following equation:

$$-\sum_{i=1}^{\infty} \varepsilon^i \boldsymbol{R}_N^{-1}\boldsymbol{G}\frac{\mathrm{d}\boldsymbol{V}^{(i-1)}}{\mathrm{d}t} = \sum_{i=1}^{\infty} \varepsilon^i \boldsymbol{V}^{(i)}. \tag{19}$$

Note that $\boldsymbol{V}^{(0)}$ depends on time only via the spatial coordinates $\boldsymbol{X}$, which allows us to write

$$\frac{\mathrm{d}\tilde{\boldsymbol{V}}^{(0)}}{\mathrm{d}t} = \frac{\partial \boldsymbol{V}^{(0)}}{\partial x_j}\frac{\mathrm{d}x_j}{\mathrm{d}t} = \boldsymbol{V}\cdot\boldsymbol{\nabla}\boldsymbol{V}^{(0)} = [\boldsymbol{V}^{(0)} + \varepsilon\boldsymbol{V}^{(1)} + \ldots]\cdot\boldsymbol{\nabla}\boldsymbol{V}^{(0)}, \tag{20}$$

where $\boldsymbol{\nabla}$ here denotes the generalized gradient operator in the (x, z, θ) space. The above equation in combination with (15) gives the following solution for the first-order function $\boldsymbol{V}^{(1)}$:

$$-\boldsymbol{R}_N^{-1}\boldsymbol{G}\boldsymbol{V}^{(0)}\cdot\boldsymbol{\nabla}\boldsymbol{V}^{(0)} = \boldsymbol{V}^{(1)}. \tag{21}$$

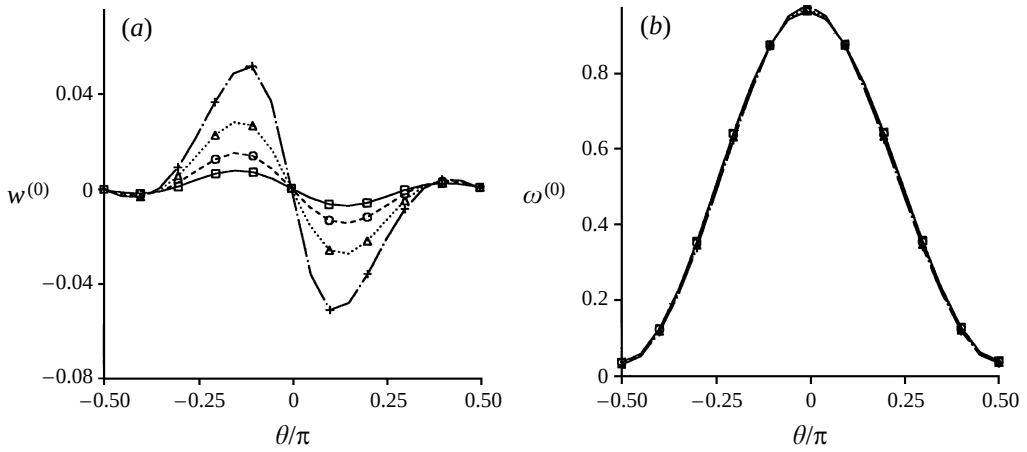

FIGURE 7. Coefficient functions of small-inertia solution, $a/c = 0.2$: (*a*) $w^{(0)}$; (*b*) $\omega^{(0)}$. □, $z = 2.0$; ○, $z = 1.5$; △, $z = 1.2$; +, $z = 1.03$.

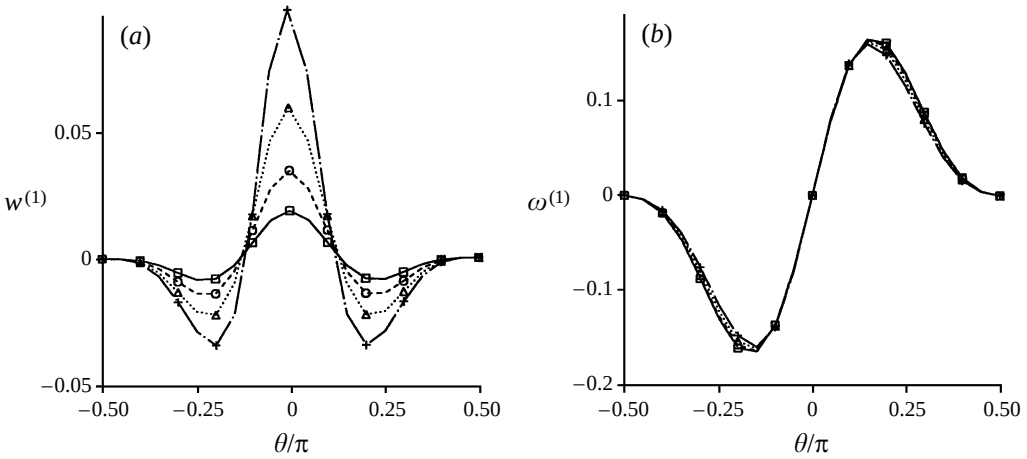

FIGURE 8. Coefficient functions of small-inertia solution, $a/c = 0.2$: (*a*) $w^{(1)}$; (*b*) $\omega^{(1)}$. □, $z = 2.0$; ○, $z = 1.5$; △, $z = 1.2$; +, $z = 1.03$.

Since $\boldsymbol{V}^{(0)}$ is explicitly independent of the coordinate x, the dot product term in (21) may be rewritten in the form

$$\boldsymbol{V}^{(0)} \cdot \boldsymbol{\nabla} \boldsymbol{V}^{(0)} = \begin{pmatrix} \partial u^{(0)}/\partial z & \partial u^{(0)}/\partial \theta \\ \partial w^{(0)}/\partial z & \partial w^{(0)}/\partial \theta \\ \partial \omega^{(0)}/\partial z & \partial \omega^{(0)}/\partial \theta \end{pmatrix} \begin{pmatrix} u^{(0)} \\ \omega^{(0)} \end{pmatrix}. \tag{22}$$

The equations for the higher-order members may be obtained from (19) in a similar way, by preserving the dependence on (z, θ) only:

$$-\boldsymbol{R}_N^{-1}\, \boldsymbol{G}(\boldsymbol{V}^{(0)} \cdot \boldsymbol{\nabla} \boldsymbol{V}^{(1)} + \boldsymbol{V}_1^{(1)} \cdot \boldsymbol{V}^{(0)}) = \boldsymbol{V}^{(2)}, \tag{23}$$

$$-\boldsymbol{R}_N^{-1}\, \boldsymbol{G}(\boldsymbol{V}^{(0)} \cdot \boldsymbol{\nabla} \boldsymbol{V}^{(2)} + \boldsymbol{V}^{(1)} \cdot \boldsymbol{\nabla} \boldsymbol{V}^{(1)} + \boldsymbol{V}^{(2)} \cdot \boldsymbol{\nabla} \boldsymbol{V}^{(0)}) = \boldsymbol{V}^{(3)}, \text{ etc.} \tag{24}$$

Equations (18), (21), (23) and (24) were solved numerically in the ranges of parameters $z < 10$, $-\pi/2 < \theta < \pi/2$. Figures 7 and 8 show the components $w^{(0)}$, $\omega^{(0)}$, $w^{(1)}$, $\omega^{(1)}$ as functions of orientation at different values of z. The zero-order functions

in fact represent the instantaneous 'lift' and rotational velocities of inertialess particles (Gavze & Shapiro 1997). One can see that $\omega^{(0)}$ and $w^{(1)}$ are symmetric functions, and $\omega^{(1)}$ and $w^{(0)}$ antisymmetric functions, of θ. This observation may be generalized to claim that $\omega^{(n)}$ and $w^{(n+1)}$ are symmetric for even n and antisymmetric for odd n.

We further use the kinematic parameters represented within the coefficient functions of expansion (17) to estimate the particle drift towards the wall. Consider a particle rotating at a certain distance z from the wall. We will estimate the drift by calculating the particle 'virtual displacement' in the z-direction from $t = 0$, corresponding to $\theta = -\pi/2$, up to the current time t:

$$\Delta z(t) = \int_0^t w|_{z=\text{const}}\, \mathrm{d}t. \tag{25}$$

In the above the integration is performed with w evaluated at a constant z, which in fact does not yield the true drift, since the particle centre moves in an oscillatory manner with increasing z. However, bearing in mind the smallness of the drift velocity and the relatively weak dependence of w on z, the above expression can be used as a fair estimate of the true drift.

Changing the integration variable $\mathrm{d}t = \mathrm{d}\theta/\omega$ in (25) one obtains

$$\Delta z(\theta) = \int_{-\pi/2}^{\theta} \left.\frac{w}{\omega}\right|_{z=\text{const}} \mathrm{d}\theta. \tag{26}$$

Substituting (17) in the term w/ω and expanding it in powers of ε, one obtains

$$\frac{w}{\omega} = \frac{\delta z^{(0)}}{\delta\theta} + \varepsilon\frac{\delta z^{(1)}}{\delta\theta} + \varepsilon^2\frac{\delta z^{(2)}}{\delta\theta} + \cdots + \varepsilon^n\frac{\delta z^{(n)}}{\delta\theta} + \cdots, \tag{27}$$

wherein

$$\frac{\delta z^{(0)}}{\delta\theta} = \frac{w^{(0)}}{\omega^{(0)}}, \tag{28}$$

$$\frac{\delta z^{(1)}}{\delta\theta} = \frac{w^{(1)}}{\omega^{(0)}} - \frac{\omega^{(1)}w^{(0)}}{(\omega^{(0)})^2}, \tag{29}$$

$$\frac{\delta z^{(2)}}{\delta\theta} = \frac{w^{(2)}}{\omega^{(0)}} - \frac{\omega^{(1)}w^{(1)} + \omega^{(2)}w^{(0)}}{(\omega^{(0)})^2} + \frac{(\omega^{(1)})^2 w^{(0)}}{(\omega^{(0)})^3}, \text{ etc.} \tag{30}$$

Bearing in mind the symmetry properties of $\boldsymbol{V}^{(i)}$, one can easily show that $\delta z^{(n)}/\delta\theta$ is an antisymmetric function of θ for even n and a symmetric function for odd n.

Clearly, the antisymmetric terms represented by $\delta z^{(0)}/\delta\theta$, $\delta z^{(2)}/\delta\theta$ do not contribute to the virtual drift, as expressed by (26), since the corresponding integrals over the orientation vanish. It is only the terms with odd n: $\delta z^{(1)}/\delta\theta, \delta z^{(3)}/\delta\theta$, etc., that may cause a drift. Figure 9(a, b) shows the contributions $\Delta z^{(n)}$, $n = 0, 1$ to the virtual drift, as functions of θ. The displacement of inertialess particles $\Delta z^{(0)}$ vanishes after a cycle, i.e. at $\theta = \pi/2$, as does $\Delta z^{(2)}$. On the other hand, the first-order contribution $\Delta z^{(1)}$ to the virtual displacement does not vanish upon completion of a cycle, but rather obtains negative values, thereby indicating the existence of a non-zero particle drift towards the wall. A similar behaviour was obtained for $\Delta z^{(3)}$ (not shown here).

Examining expression (29) for the leading first-order contribution to the virtual drift, one can see that the inertial drift is caused by two terms: the first term, $w^{(1)}/\omega^{(0)}$, is associated with the effect of inertia on the instantaneous lift velocity w, and the second term is associated with the effect of inertia on particle rotational velocity ω. Figures 7

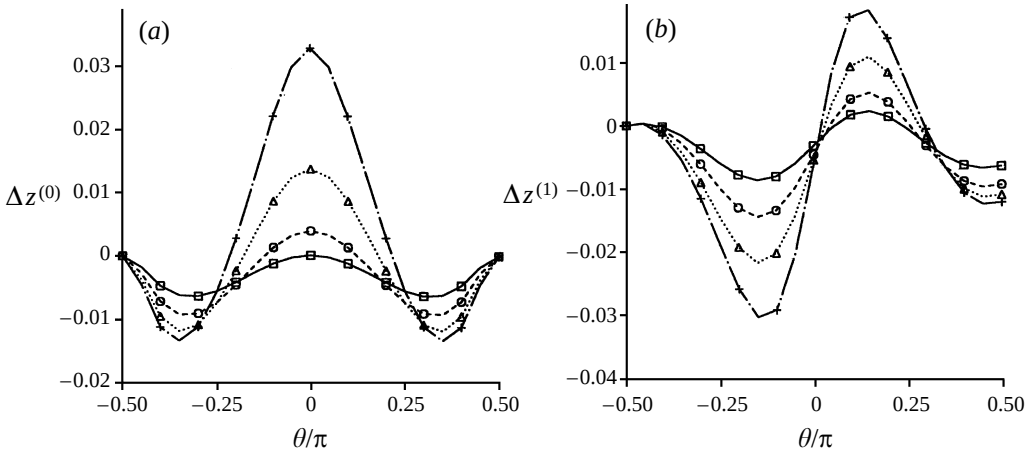

FIGURE 9. Drift function of small-inertia solution, $a/c = 0.2$: (*a*) zero-order approximation, (*b*) first-order approximation. □, $z = 2.0$; ○, $z = 1.5$; △, $z = 1.2$; +, $z = 1.03$.

and 8 show that the inertia-dependence of the lift velocity causes particle drift towards that wall (negative drift), whereas the inertia dependence of the rotation velocity causes drift from the wall (positive drift).

Consider the negative drift caused by the inertia-dependence of the instantaneous lift velocity, represented by $w^{(1)}$. To clarify its origin consider particle motion from $\theta_1 = -\pi/2$ (when its longer axis is parallel to the wall) to the upright orientation $\theta_2 = 0$ (see figures 7 and 8). At θ_1 the particle has zero first-order rotational and lift velocities. At $\theta \sim -\pi/4$, $w^{(1)}$ has a negative maximum and vanishes again at $\theta \sim -\pi/8$. Therefore the inertia slows down the particle rise during its motion from θ_1 up to about $\theta = -\pi/8$, and accelerates its rise during the rest of the period (see figure 8*a*). Since in the former period the particle has a smaller angular velocity than during the latter period (see figure 7*b*), the total effect of inertia on w is to cause the negative lift tendency, i.e. towards the wall.

Consider now the positive drift caused by the effect of inertia on particle rotational velocity, represented by $\omega^{(1)}$. The effect of inertia is to slow down particle rotation ($\omega^{(1)}$ is negative) for negative angles of attack (from $\theta_1 = -\pi/2$ to $\theta_2 = 0$) and to accelerate its rotation for positive angles of attack (see figure 8*b*). In the former period inertialess particles drift away from the wall and in the latter period towards the wall mainly due to the lift force F_z. Hence, as a result of the inertia effect on rotation, the particle has less time to go down during the latter period (with positive angles of attack) and more time to go up during the former period, which sums to yield the upward drift tendency.

It turns out that of the two tendencies described above, the lift towards the wall caused by $w^{(1)}$, i.e. by the inertia dependence of the instantaneous lift velocity, is the dominant phenomenon. Analysis of the terms of different orders in particle trajectories shows that for $\varepsilon \leqslant 0.4$ the main contribution is given by the first-order approximation. This clarifies the results on the drift velocity, given in figures 3 and 4, showing that for $\tau s < 80$, w_d changes almost linearly with τs for $\gamma < 0.5$. For $\tau s < 10$ this is true for almost all values of γ. Indeed, in the above range of τs the main contribution to the drift is given by the first-order term of expansion (17).

Equation (15) can be used to quantify the role of the initial conditions, i.e. particle initial orientation and position, on its trajectory. These initial data are 'forgotten' during one rotational period T, if ε, appearing on the left-hand side of (15) is less than T. For negligible inertia $T = \pi(\gamma + 1/\gamma)$, and $T = 2\pi$ for large inertia. For $\gamma = 0.2$ the

condition $\varepsilon < T$ implies that $\tau s < 2500$ (see table 2). Therefore the effect of the initial conditions could be observed only at very large τs (see figure 2(f), where $\tau s = 5000$), which is nevertheless, achievable for Stokesean particles, i.e. moving with Re less than unity (see §6 below).

6. Discussion and estimates

We analysed the motion of non-spherical particles in a shear flow near a plane wall, as governed by the combined effect of the particle shape, the wall effect and the particle inertia. The fluid inertia is neglected and the flow is assumed to satisfy the Stokes equation. Particle trajectories are computed from the equations of their rotation–translational motion. An efficient numerical method is employed for the calculation of trajectories. This method is based on pre-calculation of the hydrodynamic forces acting on a particle at different locations and orientations. A generalized non-dimensional inertia parameter, governing the particle motion, is defined. This parameter, which takes into account the particle shape, is the product of the particle relaxation time, shear rate and a non-dimensional function dependent on the particle resistance matrix near the wall.

The combined effect of the particle non-sphericity and of the wall proximity creates a complex system of hydrodynamic forces and torques acting on the spheroids. These interactions in combination with particle inertia result in particle drift towards the wall. This drift stems from the orientational asymmetry of the particle angular velocity and of the cross-stream velocity component w, introduced by the inertial effect. The drift is observed even for particles with very small inertia. For all γ the drift velocity has a maximum at about the same value of the generalized inertia parameter $\varepsilon = \gamma^2 N(\gamma)\tau s$. Beyond the maximal value of $\varepsilon \sim 4$ the drift velocity diminishes again.

Our calculations and analysis show that prolate spheroidal particles always drift towards the wall. An interesting question is whether all non-spherical particles drift towards the wall, or alternatively, are there particle shapes which drift in the opposite direction. To answer this question extensive calculation should be performed, including in particular oblate spheroidal particles.

The order of magnitude of the (dimensional) maximal drift force of particles with $a/c = 0.2$–0.7 as elucidated from figure 5, prevails for $\gamma^2\tau s = 20$–80 and is given by

$$w_d = (1\text{–}3) \times 10^{-3} cs.$$

For neutrally buoyant particles, where gravity does not influence particle motion the present analysis does not apply. This is because we neglected any influence of the fluid inertia, while accounting for the particle inertia. For airborne particles such an assumption is reasonable due to the smallness of the air-to-particle density. When the fluid density is comparable with that of the particle, both the flow and the particle inertia should be taken into account. In order to use the creeping flow approximation for neutrally buoyant particles, one should, therefore keep the parameters τs well below unity. In this range the drift velocity is (see figure 3) $w_d \sim 10^{-5} cs$.

We will estimate the value of the particle drift in the shear flow within the laminar sublayer of a turbulent air flow in a pipe. Taking the mean air velocity as 15 m s^{-1} and the pipe diameter as 0.1 m, one obtains the shear rate s of about 1500 s^{-1}. For this shear rate the drift velocity of spheroidal particles of density close to that of water and having the sizes 1, 10 and 30 μm are listed in table 3. For comparison we also list the characteristic Péclet number, based on the particle drift, as well as the gravitational velocity and the lift velocity induced by fluid inertia in the shear flow, both calculated

Particle size c (μm)	Reynolds number, $Re = c^2 s/\nu$	Non-dimensional relaxation time, τs	Drift velocity (μm s^{-1})	Drift Péclet number $v_d c/D$	Gravitational settling velocity (μm s^{-1})	Velocity induced by flow inertial (μm s^{-1})
1	0.0001	0.42	0.006	0.00044	150	0.33
10	0.01	45	0.6	4.4	14,000	33
30	0.09	380	144	9500	135,000	300

TABLE 3. Drift velocity of spheroidal particles in air at atmospheric pressure: $\rho_p/\rho = 1000$, $a/c = 0.3$, $z/c = 1.5$ shear rate $s = 1500$ s^{-1}, compared with the Brownian diffusivity and gravitational settling velocity of a sphere with diameter c having the same mass density.

for a spherical particle of radius c. The cases $Pe \gg 1$ and $Pe \ll 1$ respectively correspond to the situations where the drift velocity is larger and smaller than the characteristic velocity of the Brownian motion.

The flow-inertia induced lift has been calculated according to the formula (Saffman 1965)

$$v_i = \frac{6.46 v_r c s^{1/2}}{6\pi \nu^{1/2}}, \tag{31}$$

where v_r is the particle–fluid relative velocity, calculated near the wall according to the Goldman, Cox & Brenner (1967) expression

$$\frac{v_r}{sz} = 1 - \frac{0.7431}{0.6376 - 0.200 \ln (z/c - 1)}, \quad z/c \to 1. \tag{32}$$

One can see that for 1 and 10 μm particles the drift velocity is much smaller than the gravitational settling velocity in still air and the lift velocity. The drift of the 1 μm particle is also much slower than the diffusional transport associated with the Brownian motion of a comparable size sphere, as expressed in table 3 by the characteristic Péclet number. For 10 μm spheroids the drift velocity is comparable to the Brownian velocity. The 30 μm particles have much larger drift velocity which exceeds by about 1000 times the characteristic Brownian velocity of comparable spheres. On the other hand, the drift of this particle is comparable to the lift velocity induced by the flow inertia. One can see that the spheroidal particles considered in table 3 are sufficiently small so that the characteristic Reynolds associated with the velocity shear is much smaller than unity, which justifies the applicability of the present analyses performed with negligible fluid inertia. Note that the maximal values of τs achievable for Stokesean particles ($Re \leqslant 1$) may be as large as 5000, which, for example prevails for a spheroid with $c = 100$ μm, shear rate as in table 3 and ρ_p/ρ above 1500. Such density ratios are characteristic of atmospheric aerosols (Friedlander 1977).

One thus concludes that the wall-induced drift velocity of non-spherical particles is always smaller than the gravitational settling velocity. For particle sizes above 10 μm this drift exceeds the characteristic Brownian velocity and becomes comparable to the lift velocity induced by flow inertia.

The calculations performed so far hinge on the assumption that the particles' motion occurs in the (x, z) plane only. In fact the stability of such spheroidal particle motion should be studied, to check the validity of our analysis.

Unfortunately no experimental data on the motion of sufficiently large non-spherical particles in shear flows are available, which have been collected in the absence of

gravity. The present theory and the data given in table 3 may be used to design such experiments, where the wall-induced drift phenomenon could be best observed. In the following section we contemplate the physical circumstances where this drift can constitute an important mechanism governing transport of elongated particles.

7. Application to aerosol transport in microgravity

We have shown that our analysis is valid in the absence of external forces and for negligible fluid inertia and large particle inertia. Such systems are indeed met in practice and represented by aerosols in microgravity conditions. Aerosols particle sizes range from several nanometres to about 100 micrometres. The lower size limit depends upon the detection ability of modern measurement devices. The upper limit is imposed by the gravitational losses in the specific aerosol system considered. Submicrometre aerosol particles (those with the sizes less than about 0.5 μm) are significantly affected the Brownian motion and have a very low sedimentation rate. The micrometre-size aerosols, i.e. those exceeding 1–10 μm, have relatively large settling velocities, which makes them difficult to handle in laboratory studies. An aerosol investigation in microgravity conditions allows their settling velocity to be significantly reduced, and thus allows several aerosol processes to be studied, which are otherwise very difficult to investigate. Among these are several nonlinear phenomena, which have been proven to be very sensitive to gravitation. These include aerosol nucleation, coagulation, chemical reactions, and material synthesis via aerosol routes, such as hydrolysis, pyrolysis, photolysis, thermophoresis, etc. (Oostra *et al.* 1996, 1997).

The effect of reduced gravity on aerosol behaviour is two-fold. First, the absence of gravity modifies the velocity field of the carrier gas. In particular, flows induced by the buoyancy force, whenever the difference in the air density prevails, do not take place in the microgravity conditions. Secondly, the deposition rate of micrometre aerosol particles in microgravity is so low that they actually remain airborne indefinitely. This means that the concentration of such particles in air is significantly higher than that prevailing in gravity conditions. This is very important in orbital manned space stations, where aerosol particles are constantly produced in the course of various activities. Since they do not settle fast enough the risk of their inhalation by humans or animals is large. The risk assessment for these particles being deposited in the respiratory tract involves evaluation of the particle deposition rates. Normally the deposition of the relatively large micrometre particles is dominated by gravitation in the alveolar region and inertia in the airway bifurcation areas (Vincent 1995; Balàshàzy & Hofmann 1993; Kim & Iglesias 1989). The latter mechanism dominates the deposition rate of particles with sizes 1–10 μm in the microgravity conditions.

Non-spherical particles, in particular fibrous aerosols, have been identified as a special case in occupational health studies because of the serious risks associated with their inhalation. The deposition of such particles in human airways in the absence of gravitation has been attributed mainly to geometric interception in the bifurcation regions (Vincent 1995). In this respect, the inertial drift of non-spherical particles evaluated in this study constitutes an additional mechanism which can cause and even dominate their deposition in the tracheobronchial tract. Our model is applicable for calculation of deposition velocities, caused by the particle drift, in the absence of gravitation. Indeed, for the highest possible breathing rates (of about 30 litres per minute), the shear rates in the large airways (just below the larynx) are well below 1000 s^{-1}, which for particles of as large as 10 μm yields Re below 0.01. On the other hand, as shown in table 3, for the particles above 10 μm the effect of the wall-induced

drift prevails over that of Brownian motion and competes with the lift velocity induced by air inertia.

This research was supported by the Fund for the Promotion of Research at the Technion.

Appendix. Equation of rotation of spheroidal particles far from the wall

The equation of particle rotation is the third equation of the system (5). Far from the wall the coupling components $C_{\alpha\beta}$ vanish and the equation takes the following non-dimensional form: (primes are omitted):

$$\frac{\gamma^2\tau s}{5}(1+\gamma^2)\frac{\mathrm{d}\omega}{\mathrm{d}t} = L_y - \Omega_{yy}\,\omega. \tag{A 1}$$

The rotation tensor component Ω_{yy} is

$$\Omega_{yy} = \frac{16\pi\gamma^2}{3}\frac{1+\gamma^2}{\gamma^2\alpha+\beta}, \tag{A 2}$$

where

$$\alpha = \frac{1}{1-\gamma^2} - \frac{\gamma^2}{2(1-\gamma^2)^{3/2}}\ln\left[\frac{1+(1-\gamma^2)^{1/2}}{1-(1-\gamma^2)^{1/2}}\right], \tag{A 3}$$

$$\beta = -\frac{2\gamma^2}{1-\gamma^2} + \frac{\gamma^2}{(1-\gamma^2)^{3/2}}\ln\left[\frac{1+(1-\gamma^2)^{1/2}}{1-(1-\gamma^2)^{1/2}}\right]. \tag{A 4}$$

The torque acting on a particle is (see Appendix A of Gavze & Shapiro 1997)

$$L_y = \frac{\Omega_{yy}}{1+\gamma^2}(\cos^2\theta + \gamma^2\sin^2\theta). \tag{A 5}$$

Substituting L_y and Ω_{yy} in equation (A 1) and rearranging terms, one gets

$$\tau s A(\gamma)\frac{\mathrm{d}\omega}{\mathrm{d}t} + \omega = \frac{1}{2}\left(\frac{1-\gamma^2}{1+\gamma^2}\cos 2\theta + 1\right), \tag{A 6}$$

where

$$A(\gamma) = \frac{3(\gamma^2\alpha+\beta)}{80\pi}. \tag{A 7}$$

Examination of expressions (A 3) and (A 4) for α and β shows that in the limit of small γ the effect of particle shape on its rotation is governed by the parameter $A(\gamma)\tau s$, with $A(\gamma)$ being proportional to γ^2.

REFERENCES

Asgharian, B. & Anjilvel, S. 1995 The effect of fiber inertia on its orientation in a shear flow with application to lung dosimetry. *Aerosol Sci. Technol.* **23**, 282–290.

Balàshàzy, I. & Hofmann, W. 1993 Particle deposition in airway bifurcations – I. Inspiratory flow. 1993 *J. Aerosol Sci.* **24**, 745–772.

Broday, D., Fichman, M., Shapiro, M. & Gutfinger, C. 1998 Motion of spheroidal particles in vertical shear flows. *Phys. Fluids* **10**, 86–100.

Feng, J., Huang, P. Y. & Joseph, D. D. 1995 Dynamic simulation of the motion of capsules in pipelines. *J. Fluid Mech.* **286**, 201–227.

Feng, J. & Joseph, D. D. 1995 The unsteady motion of solid bodies in creeping flows. *J. Fluid Mech.* **303**, 83–102.

Friedlander, S. K., 1977 *Smoke, Dust and Haze. Fundamentals of Aerosol Behavior*. J. Wiley & Sons.

Gavze, E. & Shapiro, M. 1996 Sedimentation of spheroidal particles in vertical shear flow. *J. Aerosol Sci.* **27**, S585–586.

Gavze, E. & Shapiro, M. 1997 Particles in a shear flow near a solid wall: Effect of nonsphericity on forces and velocities. *Intl J. Multiphase Flow* **23**, 155–182.

Goldman, A. J., Cox, R. J. & Brenner, H. 1967 Slows viscous motion of a sphere parallel to a plane wall II. Couette flow. *Chem. Engng Sci.* **22**, 653–660.

Happel, J. & Brenner, H. 1983 *Low Reynolds Number Hydrodynamics*. Martinus Nijhoff.

Ho, B. P. & Leal, L. G. 1974 Inertial migration of rigid spheres in two-dimensional unidirectional flows. *J. Fluid Mech.* **65**, 365–400.

Holländer, W. 1993 Aerosols and microgravity. *Adv. Colloid Interface Sci.* **46**, 49–57.

Holländer, W. 1996 Aerosol experiments under microgravity conditions. *ESA Symp. Proc. on Space Station Utilization, ESOC, Darmstadt, December 1996*, pp. 309–312.

Huang, P. Y., Feng, J. & Joseph, D. D. 1994 The turning couples on an elliptic particle settling in a vertical channel. *J. Fluid Mech.* **271**, 1–16.

Jeffery, G. B. 1922 The motion of Ellipsoidal particles immersed in viscous fluid. *Proc. R. Soc. Lond.* A **102**, 161–179.

Karnis, A., Goldsmith, H. & Mason, S. G. 1963 Axial migration of particles in Poiseuille flow. *Nature* **200**, 159–160.

Karnis, A., Goldsmith, H. & Mason, S. G. 1966 The flow of suspensions through tubes. V Inertial effects. *Can. J. Chem. Engng* **44**, 181–193.

Kim, C. S. & Iglesias, A. J. 1989 Deposition of inhaled particles in bifurcating airway models: I Inspiratory deposition. *J. Aerosol Med.* **2**, 1–14.

Oostra, W., Bryant, D., Marijnissen, J. C. M., Scarlett, B. & Wissenburg, J. 1996 Measurement of soot production of a candle under microgravity conditions. *J. Aerosol Sci.* **27**, S715–716.

Oostra, W., Marijnissen, J. C. M., Scarlett, B. & Bryant, D. 1995 A comparison of thermophoresis in a laminar flow under gravity and microgravity conditions. *J. Aerosol Sci.* **26**, S317–318.

Saffman, P. G. 1965 The lift on a small sphere in a slow shear flow. *J. Fluid Mech.* **22**, 385–400; and corrigendum **31** (1968), 624.

Schonberg, J. A. & Hinch, E. J. 1989 The inertial migration of a sphere in Poiseuille flow. *J. Fluid Mech.* **203**, 517–524.

Segré, G. & Silberberg, A. 1962*a* Behaviour of macroscopic rigid spheres in Poiseuille flow. Part 1. Determination of local concentration by statistical analyses of particle passages through crossed light beams. *J. Fluid Mech.* **14**, 115–135.

Segré, G. & Silberberg, A. 1962*b* Behaviour of macroscopic rigid spheres in Poiseuille flow. Part 2. Experimental results and interpretation. *J. Fluid Mech.* **14**, 136–157.

Sugihara-Seki, M. 1993 The motion of an elliptical cylinder in channel flow at low Reynolds numbers. *J. Fluid Mech.* **257**, 575–596.

Vincent, J. H. 1995 *Aerosol Science for Industrial Hygienists*. Pergamon.

Yang, S. M. & Leal, G. L. 1984 Particle motion in Stokes flow near a plane fluid-fluid interface. Part 2. Linear shear and axisymmetric straining flows. *J. Fluid Mech.* **149**, 275–304.